Planetary and Space Science 57 (2009) 1671–1681

Contents lists available at ScienceDirect

Planetary and Space Science

journal homepage: www.elsevier.com/locate/pss

Saturn's north polar cyclone and hexagon at depth revealed by Cassini/VIMS

Kevin H. Baines [a,*], Thomas W. Momary [a], Leigh N. Fletcher [b], Adam P. Showman [c], Maarten Roos-Serote [d], Robert H. Brown [c], Bonnie J. Buratti [e], Roger N. Clark [f], Philip D. Nicholson [g]

[a] Jet Propulsion Laboratory, California Institute of Technology, MS 183-601, 4800 Oak Grove Drive, Pasadena, CA 91109, USA
[b] Jet Propulsion Laboratory, California Institute of Technology, MS 169-237, 4800 Oak Grove Drive, Pasadena, CA 91109, USA
[c] Lunar and Planetary Laboratory, University of Arizona, Tucson, AZ 85721, USA
[d] Observatorio Astronomico de Lisboa, Tapada da Ajuda, 1349-018 Lisboa, Portugal
[e] Jet Propulsion Laboratory, California Institute of Technology, MS 183-501, 4800 Oak Grove Drive, Pasadena, CA 91109, USA
[f] US Geological Survey, MS 964, Box 25046 Federal Center, Denver, CO 80225, USA
[g] Cornell University, Astronomy Department, Space Sciences Building, Ithaca, NY 14853, USA

ARTICLE INFO

Article history:
Received 17 November 2008
Received in revised form
18 May 2009
Accepted 12 June 2009
Available online 4 July 2009

Keywords:
Saturn
Cassini–Huygens
Visual-infrared mapping spectrometer (VIMS)
Atmospheric dynamics
Polar cyclone
Saturn clouds

ABSTRACT

A high-speed cyclonic vortex centered on the north pole of Saturn has been revealed by the visual-infrared mapping spectrometer (VIMS) onboard the Cassini–Huygens Orbiter, thus showing that the tropospheres of both poles of Saturn are occupied by cyclonic vortices with winds exceeding 135 m/s. High-spatial-resolution (~200 km per pixel) images acquired predominantly under night-time conditions during Saturn's polar winter—using a thermal wavelength of 5.1 μm to obtain time-lapsed imagery of discrete, deep-seated (>2.1-bar) cloud features viewed in silhouette against Saturn's internally generated thermal glow—show a classic cyclonic structure, with prograde winds exceeding 135 m/s at its maximum near 88.3° (planetocentric) latitude, and decreasing to <30 m/s at 89.7° near the vortex center and <20 m/s at 80.5°. High-speed winds, exceeding 125 m/s, were also measured for cloud features at depth near 76° (planetocentric) latitude within the polar hexagon consistent with the idea that the hexagon itself, which remains nearly stationary, is a westward (retrograde) propagating Rossby wave – as proposed by Allison (1990, Science 247, 1061–1063) – with a maximum wave speed near 2-bars pressure of ~125 m/s. Winds are ~25 m/s stronger than observed by Voyager, suggesting temporal variability. Images acquired of one side of the hexagon in dawn conditions as the polar winter wanes shows the hexagon is still visible in reflected sunlight nearly 28 years since its discovery, that a similar 3-lane structure is observed in reflected and thermal light, and that the cloudtops may be typically lower in the hexagon than in nearby discrete cloud features outside of it. Clouds are well-correlated in visible and 5.1 μm images, indicating little windshear above the ~2-bar level. The polar cyclone is similar in size and shape to its counterpart at the south pole; a primary difference is the presence of a small (<600 km in diameter) nearly pole-centered cloud, perhaps indicative of localized upwelling. Many dozens of discrete, circular cloud features dot the polar region, with typical diameters of 300–700 km. Equatorward of 87.8°N, their compact nature in the high-wind polar environment suggests that vertical shear in horizontal winds may be modest on 1000 km scales. These circular clouds may be anticyclonic vortices produced by baroclinic instabilities, barotropic instabilities, moist convection or other processes. The existence of cyclones at both poles of Saturn indicates that cyclonic circulation may be an important dynamical style in planets with significant atmospheres.

1. Introduction

Saturn's north polar region is especially mysterious due to an unusual hexagonal feature centered near 76°N. lat (planetocentric), originally discovered by Godfrey (1988). In Voyager imagery, Godfrey noted that while the clouds forming the feature move at ~100 m/s, the overall hexagonal feature remains stationary in the frame of reference defined by the periodicity of Saturnian kilometric radiation (SKR) measured by Voyager (Desch and Kaiser, 1981). Images taken by Cassini some 28 years later reveal that this feature still exists, essentially unchanged (Figs. 1 and 2). The mechanism maintaining the hexagon is poorly understood; a Rossby wave mechanism has been proposed (Allison et al., 1990), wherein a perturbed zonal jet oscillates latitudinally in response to the restoring force of the latitudinally varying Coriolis effect. A dark spot outside of the

* Corresponding author. Tel.: +1818 354 0481; fax: +1818 952 0475.
E-mail addresses: kevin.baines@jpl.nasa.gov (K.H. Baines), thomas.w.momary@jpl.nasa.gov (T.W. Momary), Leigh.N.Fletcher@jpl.nasa.gov (L.N. Fletcher), showman@lpl.arizona.edu (A.P. Showman), planet.mrs@gmail.com (M. Roos-Serote), rhb@lpl.arizona.edu (R.H. Brown), bonnie.buratti@jpl.nasa.gov (B.J. Buratti), rclark@usgs.gov (R.N. Clark), nicholso@astro.cornell.edu (P.D. Nicholson).

0032-0633/$ - see front matter © 2009 Elsevier Ltd. All rights reserved.
doi:10.1016/j.pss.2009.06.026

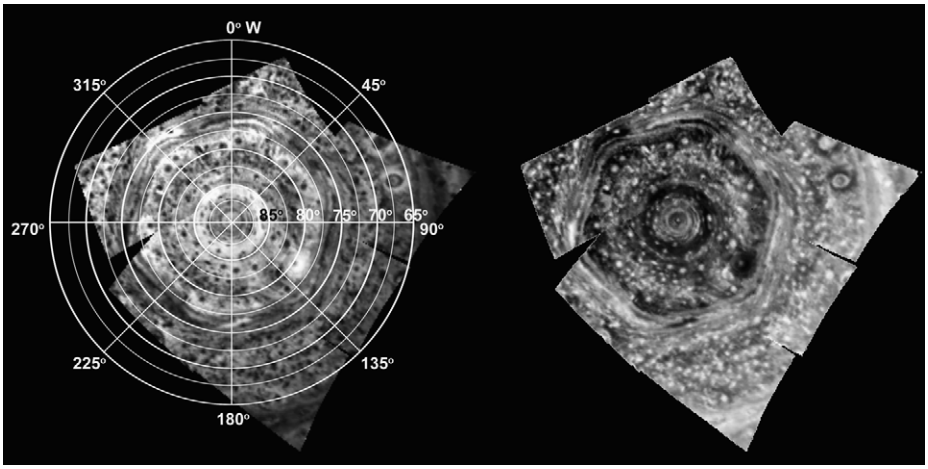

Fig. 1. High-spatial-resolution (211 km per pixel) polar orthographic projection of a mosaic of nine 5.1-μm images of Saturn's north polar region. Positive image (left), obtained under night-time conditions, depicts polar clouds (dark) as viewed in silhouette against Saturn's 5.1 μm thermal emission. Photometrically inverted version (right) shows clouds as bright. For scale, a planetocentric latitudinal/longitudinal grid is superimposed on the 5.1 μm thermal flux image. Images obtained June 15, 2008 from a mean distance of 0.352 million km and mean sub-spacecraft latitude of 70.9°N.

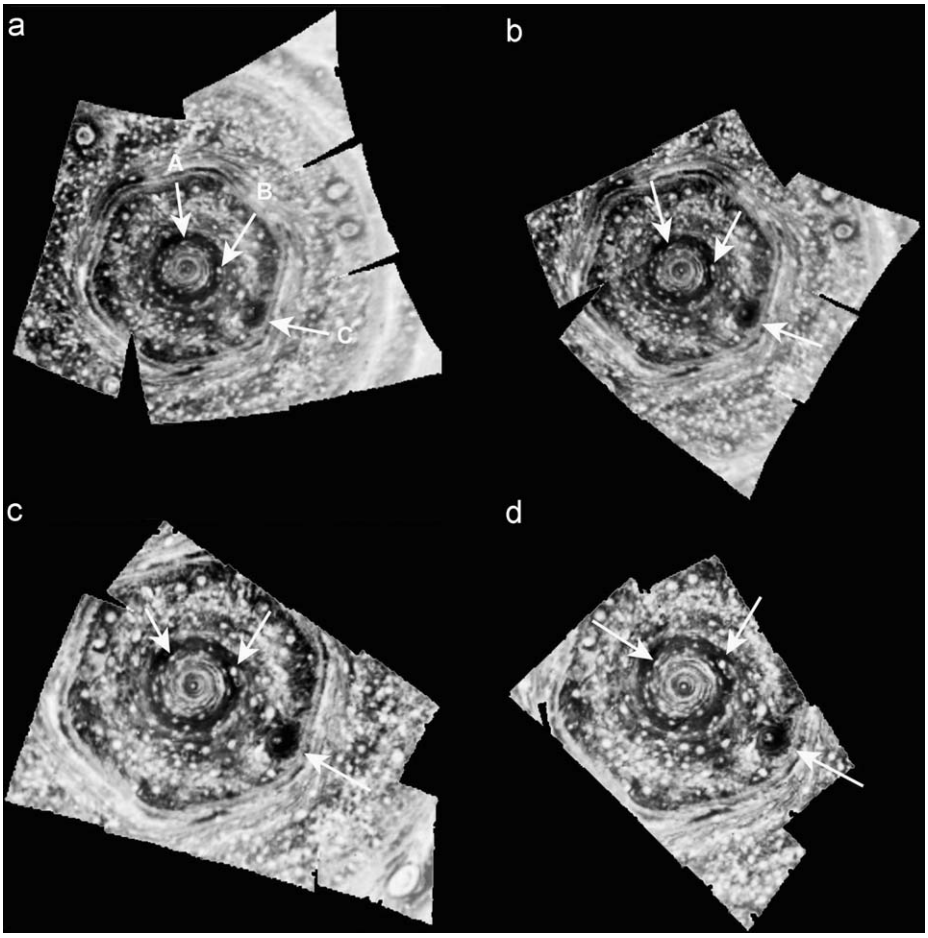

Fig. 2. Set of four high-spatial-resolution 5.1-μm mosaics of Saturn's north polar region, photometrically inverted to show clouds as bright features. These near-nadir views (sub-spacecraft latitude: 64–75°) were acquired progressively on June 15, 2008 over a 6-h period from close range (as close as 224,000 km above the 1-bar level), yielding clear polar views with up to 112 km/pixel resolution. Arrows point to clouds at three different latitudes, showing that winds are prograde and vary widely in speed over latitude within the vortex.

hexagon has been suggested as the source of the perturbation (Allison et al., 1990). Such a feature was seen repeatedly more than a decade later in ground-based and Hubble Space Telescope imagery (Sánchez-Lavega et al., 1993, 1997) but not in recent Cassini/VIMS imagery (e.g., Fig. 1 and 2). As well, no evidence of such a feature was observed in Cassini/CIRS infrared imagery obtained in March, 2007 (Fletcher et al., 2008).

Thus far, little information has been obtained about the far north, inside the hexagon. In particular, sparse information exists on dynamical features that might bear on the processes forming

and maintaining the hexagon. As well, although a cyclonic hot vortex has been demonstrated to exist at the north pole in the upper troposphere and stratosphere by thermal-IR imaging (Fletcher et al., 2008), it is not known whether the vortex demonstrates cloud morphologies and wind speeds similar to the south polar cyclone (Dyudina et al., 2008, 2009).

2. Observations and zonal-wind results

We report the first measurements of zonal winds throughout the north polar region, showing that a cyclonic vortex exists at the pole. These observations complement cloud tracking performed on VIMS images at lower latitudes (Choi et al., 2009). As shown in Table 1, mosaics of the polar region north of ~70°N were acquired four times on June 15–16, 2008 by the visual-infrared mapping spectrometer (VIMS) onboard the Cassini spacecraft orbiting Saturn. These mosaics were obtained at high-spatial-resolution (as small as 122 km in the instrument's instantaneous field of view, IFOV) over a range 0.224–0.442 million km above the clouds from a vantage point high over northern latitudes (sub-spacecraft latitudes of 64°–75° N. latitude). While, typically, the VIMS instrument simultaneously acquires images in 352 wavelength bands from 0.35 to 5.1 μm (c.f. Brown et al., 2004 for an instrument review), we concentrate here on 5.1-μm thermal imagery and associated 4.6–5.1-μm spectra observable under the predominantly night-time conditions of the north polar region extant in June, 2008.

All images were photometrically and geometrically calibrated, including de-spiking and flat-fielding, using the well-developed procedures of the VIMS Science Team as outlined in Barnes et al. (2007). In particular, images were geometrically calibrated using the ISIS software procedures (Gaddis et al., 1997) at the VIMS data processing center at the University of Arizona, using the post-observation Cassini Mission SPICE kernels generated by NASA/JPL. A 0.2-mrad navigational uncertainty in both the latitudinal and longitudinal components was adopted in the analysis of feature position and zonal wind, as determined in a test of VIMS latitude/longitude assignments against those determined by RADAR, taken as ground truth, for an array of features on Titan (Lawrence Soderblom, personal communication).

As shown in Fig. 1, the 5.1-μm thermal imagery reveals zonally oriented structures in the polar region, virtually all the way north to the pole. A polar ring of clouds is observed extending from 87.8°N to 88.6°N planetocentric (pc) latitude. A 5-μm-bright ring – denoting a region of reduced aerosol opacity – extends from 83° to 86.8° pc lat. At the time of these observations, the pole itself was occupied by a discrete cloud feature some 600 km in diameter. The center of this polar cloud is located at 89.7°, offset some 300 km from the exact pole. Many dozens of similarly shaped and size cloud features dot the polar region, occupying about 30% of the region.

Near 76° pc lat, the polar hexagon originally discovered by Godfrey (1988) is observed. Here, it appears predominantly as two distinctive cloud "tracks" separated by a nearly cloud-free track. This complex of three hexagonal tracks extends over about 3° of latitude at any single longitude.

We determined the polar zonal windfield from measurement of the time-varying longitudes of these cloud features as observed in four mosaics obtained over an 8.5-h period. As shown in Fig. 2, many clouds change their longitudinal position noticeably between images, particularly near the pole. Other clouds, such as those near 80° pc lat, remain nearly stationary.

The resulting zonal-wind profile over latitude is shown in Fig. 3. For each of 110 cloud points measured, the mean wind was determined by a linear fit of the longitudinal position of the feature vs. time, following the LINFIT procedure of Bevington (1969). At latitudes poleward of 80° pc lat, the longitudinal positions of features were measured in all four mosaics. Equatorward of 80° pc lat, features were frequently observed and measured in just two or three mosaics. The longitudinal uncertainty was determined from two factors: the uncertainty of 0.25 mrad for the location of a bright point within the VIMS 0.5-wide IFOV, and the 0.2 mrad uncertainty in the longitudinal component of navigation for a VIMS pixel noted earlier. Together, these effects lead to a 0.32 mrad uncertainty associated with each longitudinal (and latitudinal) position measurement. These uncertainties fold into the determination of the uncertainty of the slope of the linear fit to the time–longitude data, thereby yielding an uncertainty for each zonal-wind measurement. In Fig. 3, the displayed zonal-wind measurements are averaged over all observations within a latitude bin 0.2° wide, encompassing, typically, 2–3 points. For each binned point, the zonal-wind uncertainty, σ_{bin}, is determined by the greater of (1) the standard deviation calculated in the standard fashion, involving the square root of the sum of the squares of the difference between each

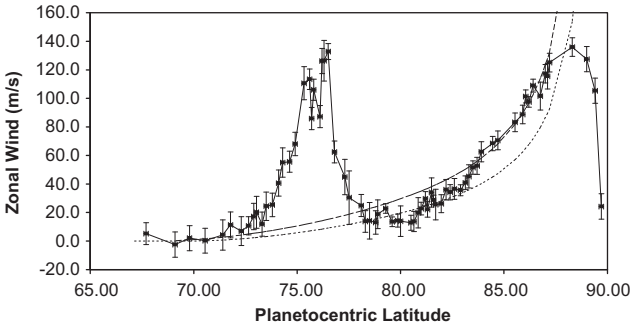

Fig. 3. Latitudinal profile of the north polar zonal winds (filled points with error bars). Model wind profiles assuming constant absolute-vorticity poleward of latitude ϕ_o yield the smooth curves, with $\phi_o = 68.0°$ (upper, long-dashed curve) and 69.5° (lower, dotted curve). Displayed error bars for the zonal winds are explained in the text.

Table 1
Summary of observations.

Mosaic #	# of VIMS frames in mosaic	Start time of first frame	End time of last frame	Range at start (10^3 km)	Sub-S/C latitude (°, pc)
	North pole				
1	9	6/15/08 16:05	6/15/08 17:38	422	64.9
2	9	6/15/08 17:48	6/15/08 19:19	374	69.2
3	12	6/15/08 20:35	6/15/08 22:27	290	75.3
4	12	6/15/08 22:39	6/16/08 0:31	224	70.9
	South pole				
1	10	6/16/08 14:51	6/16/08 17:21	405	−48.3

individual mean wind measurement and the bin-averaged mean wind, and (2) the net standard deviation calculated from all of the standard deviations, σ_i, of the individual wind measurements in the bin, according to the standard formula

$$\sigma_{bin} = [1/\sum(1/\sigma_i^2))]^{1/2}.$$

The latitudinal error bars depicted in Fig. 3 were determined in a two-step process. First, a determination was made of the greater of (1) the square root of the sum of the squares of the difference between each latitude measurement and the bin-averaged latitude and (2) the 0.25 mrad uncertainty of the latitudinal position of a point within the IFOV. Then, to account for navigational uncertainty, these values were combined with the 0.2 mrad latitudinal component of the navigational uncertainty noted above. For case (2), the combined uncertainty is 0.32 mrad, corresponding to latitudinal uncertainties from 0.08° to 0.13° for observations obtained from distances of 0.25×10^6 and 0.4×10^6 km, respectively. In Fig. 3, the combined latitudinal uncertainty pertaining to the observation made at the closest distance was used.

Fig. 3 shows the distinct structure of a polar cyclone. As summarized in Table 2, low prograde winds (<15 m/s) near 80° pc lat monotonically increase toward the pole, reaching a maximum of 136.0±6.5 m/s at 88.3° pc lat. Poleward of the cyclone wind maximum at 88.3° pc lat, the zonal winds rapidly fall off – with a latitudinal shear exceeding 0.2 m/s/km – to a speed of 24.3±8.9 m/s for the polar cloud at 89.7 ° pc lat, the most polar point measured. An analysis of the zonal-wind structure predicted by the condition that winds maintain a constant absolute vorticity poleward of 68.0° pc lat (following the analysis of Dyudina et al., 2009) yields a reasonable fit to the observed zonal-wind profile equatorward of 87° pc lat—with the notable exception of the hexagonal jet region near 76° pc lat. In a two-dimensional model, absolute vorticity tends to be conserved following the flow under adiabatic, frictionless conditions; this means that, in such a fluid, latitudinal mixing by turbulence tends to produce a homogenized absolute-vorticity profile with latitude. The near-constancy of absolute vorticity between the hexagon and the polar cyclone (Fig. 3) thus hint that mixing could be important in controlling the wind and vorticity structures in this region. However, we caution that in a three-dimensional fluid, the conserved quantity is not absolute vorticity but rather the potential vorticity (PV), which is the absolute vorticity times the gradient of potential temperature divided by density. Thus, the PV depends not only on the wind structure but on the vertical temperature gradient (a measure of the static stability of the air). Read et al. (2009) have combined cloud-level zonal-wind observations with Cassini thermal measurements to calculate latitudinal profiles of the zonal-mean PV. These profiles show a step in PV at a latitude of 75–80° (presumably associated with the hexagon), but the profiles do not extend sufficiently poleward to ascertain whether PV is homogenized closer to the polar cyclone.

Table 2
Dynamical characteristics of major features in the north polar region.

Characteristic	North cyclone	Hexagon
Latitude (pc) of maximum measured wind (°)	88.3	76.5
Maximum wind (m/s)	136.0±6.5	133.2±8.3
Latitudes (pc) of minimum measured wind (°)	80.5, 89.7	70.6, 78.8
Minimum windspeed (poleward side)	24.3±8.9	13.0±8.1
Minimum windspeed (equatorward side)	12.9±1.0	0.3±8.1
Maximum latitudinal shear (cm/s/km)	−25.8±5.9	−10.0±1.5
Latitude range of max latitudinal shear (°, pc)	89.4–89.7	76.5–77.5

Fig. 3 shows the latitudinally averaged zonal-wind structure within the hexagonal jet. A prograde jet structure is observed, with winds at 76.5° pc lat exceeding 124 m/s, comparable to the maximum winds in the cyclone. Latitudinal wind shears exceed 0.1 m/s/km on the poleward side of the jet, and, as with the cyclone, are significantly greater there than on the equatorward side.

Fig. 4 shows the measured relative vorticity, ζ, as a function of latitude, as determined by the measured zonal winds. Poleward of about 86° pc lat, the relative vorticity varies significantly with latitude, consistent with the dichotomy between the observed and modeled constant absolute-vorticity zonal-wind curves in Fig. 3. Thus, relative vorticity is not maintained inward of the maximum zonal wind, as expected for cyclonic structures where the winds must decrease to zero at the axis of the cyclone. Note that, as one crosses the latitude of the hexagon, the relative vorticity flips from strongly negative (anticyclonic) to positive (cyclonic) and back again, which may have dynamical significance.

In the polar hexagon region, multiple peaks in the averaged zonal-wind structure are displayed in Fig. 3. As shown in Fig. 5, these are artifacts of zonal-averaging, not representative of the zonal winds within the hexagonal structure. In Fig. 5, winds for prominent near-axisymmetric features within the hexagonal structure (e.g., "Inner Track", "Clear Lane", "Outer Track") are shown, with each measurement determined by averaging

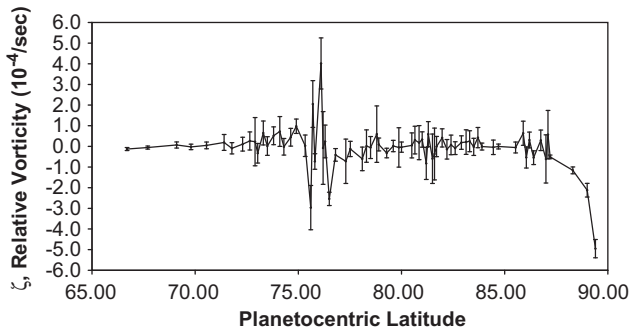

Fig. 4. Latitudinal profile of the relative vorticity, ζ, through the north polar vortex and north polar hexagon. The relative vorticity has an (absolute) maximum near the pole and falls off with latitude. Equatorward of ~87°N. latitude, the curve (with error bars) is consistent with a constant relative vorticity, except in the region of the hexagon near 76°N. (planetocentric) latitude.

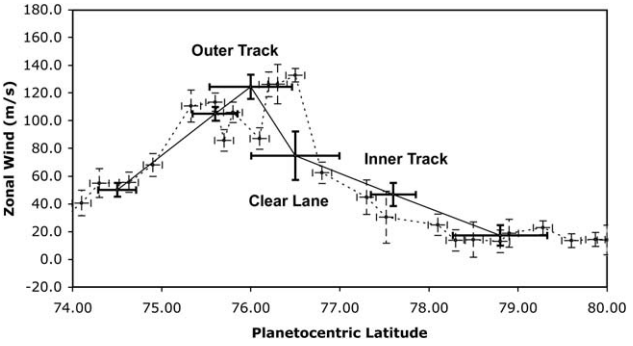

Fig. 5. Latitudinal profile of the zonal winds within the hexagonal jet. Zonal winds binned strictly by latitude (dashed) in the hexagon and its environs are compared to winds for prominent nearly axisymmetric features of the hexagon (solid). Error bars for the latitudinally averaged curve are as in Fig. 3. For each of the hexagon features (solid points with error bars), the mean latitude and wind shown are the means of the data points used in measuring that feature's characteristics, and the associated latitudinal and zonal-wind error bars represent the standard deviations of this latitudinally dispersed set of data points. The significant latitudinal undulations of the hexagonal structure results in relatively large latitudinal standard deviations, up to ~1° in extent.

numerous observations around the hexagon. Due to the latitudinally undulating nature of the hexagon, measurements over a relatively wide variety of latitudes (up to 1°) are used to determine the mean wind value. The results of such a hexagon-feature analysis shows that the region is occupied by a single jet with maximum mean zonal wind of 124.5 ± 8.7 m/s located in the outer track of the hexagon. This is some 25 m/s greater than the zonal winds reported by Godfrey (1988) from daytime cloudtop imagery, located some 75 km above the lower-level clouds tracked here, indicating a vertical shear of about 0.3 m/s/km in the troposphere between approximately 0.5 and 2-bars if zonal winds are temporally invariant in the polar hexagon. Alternatively, if the observed clouds are the same entities in visible light and at depth, as seems to be the case based on the co-alignment of the thermal and visible cloudtop features presented here (see below), and if the cloudtops are at the same altitude as the (unmeasured) cloudtops seen in reflected sunlight by Voyager, then these new wind measurements indicate time-variable winds in the hexagon. New measurements of visible cloud winds should be forthcoming as the sun rises over the hexagon, allowing some clarification of this issue.

That the clouds seen in reflected sunlight are the same as at depth has not yet been clearly established, as, in the summer of 2008, sunlight was just beginning to impinge on the hexagon at the end of north polar winter. However, as shown in Fig. 6, the first images of sunlit hexagon clouds in the Cassini era do seem to indicate that clouds observed at 5 μm are correlated with clouds seen in images acquired in reflected sunlight both at 1.6 μm – a pseudo-continuum wavelength devoid of atmospheric gas absorption – and at 0.9 μm, where atmospheric absorption by methane gas is significant. This is revealed in the combined-wavelength color image of Fig. 6 where the false color signals of clouds at each wavelength – red for 5.1 μm deep-cloud opacity, green for 1.6 μm cloud reflectivity, and blue for 0.9 μm high-altitude cloud reflectivity – are seen to overlap each other in many discrete features throughout the sunlit portion of the polar region, producing yellow–white clouds. However, the relatively muted appearance of most hexagon clouds in the methane band 0.9 μm imagery indicates that the cloudtops there may be mostly deeper than in brighter 0.9 μm-imaged clouds located 2–3° of latitude inside and outside of the hexagon. Nevertheless, at least one hexagonal cloud is as bright as neighboring features at 0.9 μm, indicating that some hexagonal clouds reach comparable altitudes as non-hexagonal discrete clouds.

Comparison of the northern and southern cyclones shows marked similarities and contrasts. Fig. 7 shows both polar

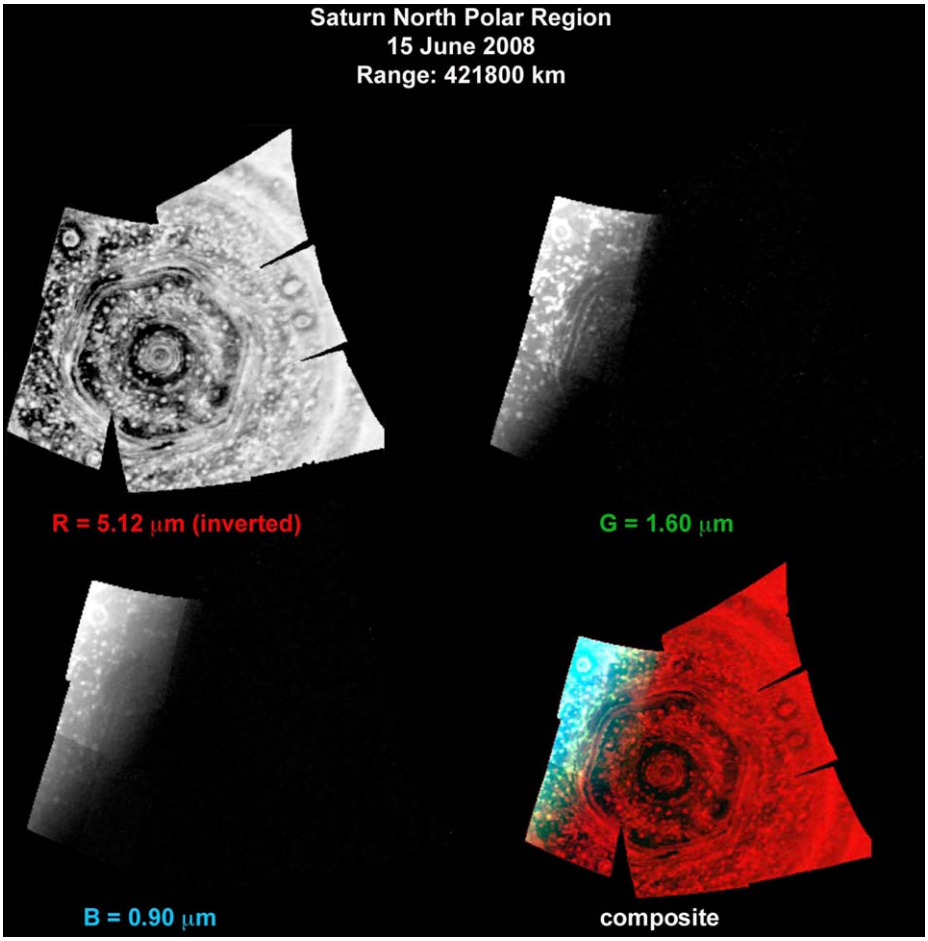

Fig. 6. Sunrise over the polar hexagon. Views acquired at solar-reflective wavelengths, 0.9 and 1.6 μm, show sunlit portion of the hexagon. The muted appearance of the hexagon vs. nearby cumulus clouds in the 0.9 μm methane-gas-absorbing wavelength indicates that the hexagon lies beneath a larger over-burden of methane-laden atmosphere – that is, it is deeper down in the atmosphere—than nearby discrete cloud features. The 1.6 μm pseudo-continuum image, unhindered by atmospheric methane absorption, clearly shows the nested nature of the hexagon, marked by two lanes of clouds divided by a third lane relatively clear of clouds. The 5.1 μm image of Saturn's thermal glow – here photometrically inverted – shows silhouetted clouds as bright areas similar to their depiction in reflected sunlight. In the color composite, white features are relatively high clouds, yellow features are deeper clouds, and red features on the daylit side are still deeper clouds. Only the reddish hue of the 5.1 μm image appears on the nightside portion of the image. Bluish color throughout the dayside indicates the presence of an optically thin, small-particle haze overlying the visible pole at high altitude.

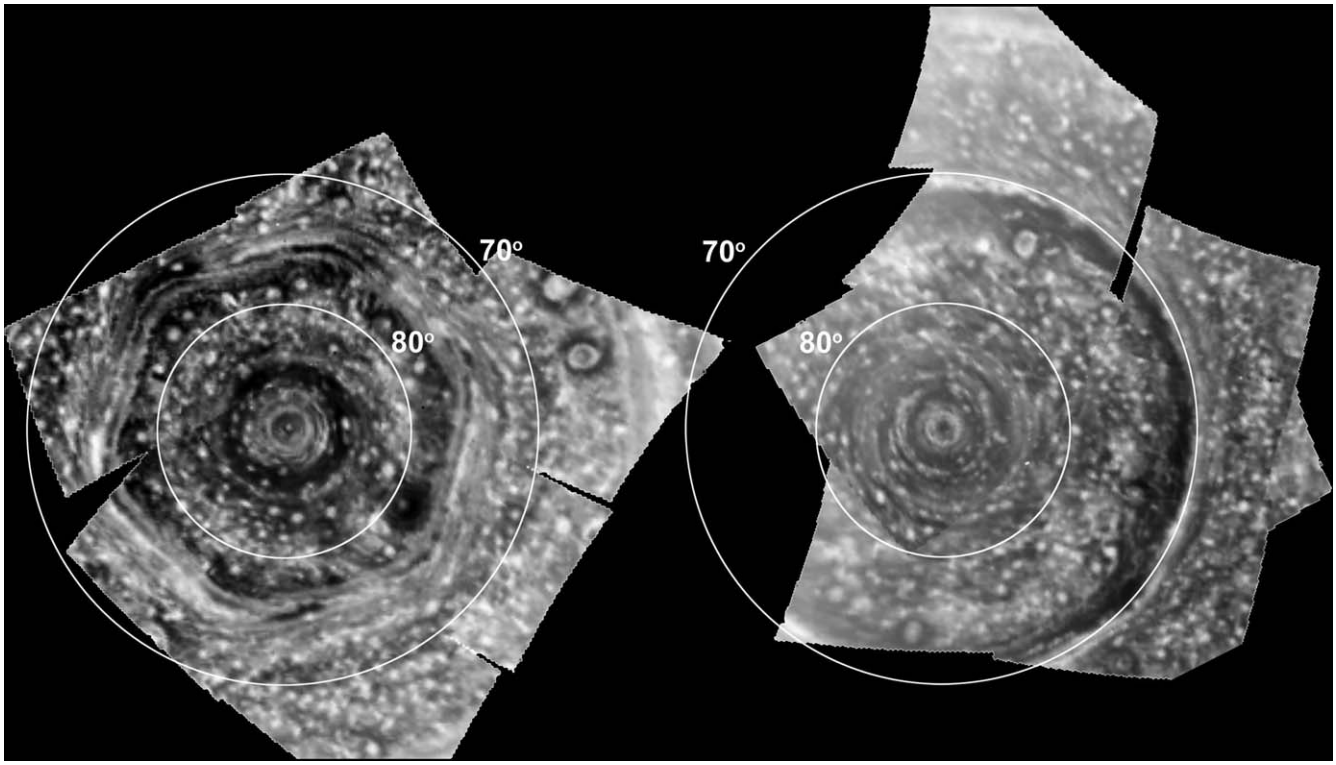

Fig. 7. North and south poles compared. Images acquired June 15, 2008 (north pole, left) and June 16, 2008 (south pole, right) show the poles at comparable resolution. Image mosaics acquired from mean ranges 0.352 (north) and 0.430 (south) million km and mean sub-spacecraft latitudes of 70.9°N. (north) and 47.5°S. latitude (south). Mean IFOV per pixel is 176 km (north) and 215 km (south).

cyclones, as obtained at comparative resolution and spatial coverage over a 25-h period, June 15–16, 2008. Both cyclones show zonal structures and comparable populations of discrete cloud features. Near the center of the cyclones, each has a cloudy ring with a width of approximately 0.5° (500 km), extending from 88.2° to 88.7°pc lat in the north and 88.5–89.0° pc lat in the south. A primary difference is that the northern cyclone shows a discrete cloud feature while the southern cyclone shows a clearing, akin to an eye of a hurricane. Another obvious difference is the hexagonal structure in the north. No similar structure is seen in the south, although near 70°S pc lat, a distinctive two-lane axisymmetric structure of a globe-encircling cloud "zone" bordered poleward by a relatively clear "belt" circles the pole. This structure spans about 3° of latitude, similar to the width of the north polar hexagon.

Fig. 8 and Table 3 compare the zonal winds of the northern and southern cyclones. The measurements indicate that the latitude of maximum winds occurs within 3° of the pole. Specifically, the maximum mean winds are measured at 88.3°N and 87.5°S, and reach speeds of 136 ± 7 and 174 ± 21 m/s for the northern and southern cyclones, respectively. However, the measurement uncertainties and sparseness of the data allow for a rather broad range of possible peak wind latitudes, spanning 87–89° in both hemispheres, For the southern cyclone, more detailed measurements of cloud-tracked winds obtained in reflected sunlight by Cassini/ISS (Dyudina et al., 2009) also indicate a broad latitudinal peak of the zonal winds, spanning 87–89°S, not inconsistent with the northern hemisphere results at 5 μm presented here. From the latitude of maximum winds equatorward for about 7° of latitude, the winds in the southern cyclone are about 30 m/s stronger than the northern cyclone. The notably weaker wind structure measured in the northern cyclone is consistent with the Cassini/CIRS thermal wind results pertaining to higher atmospheric levels

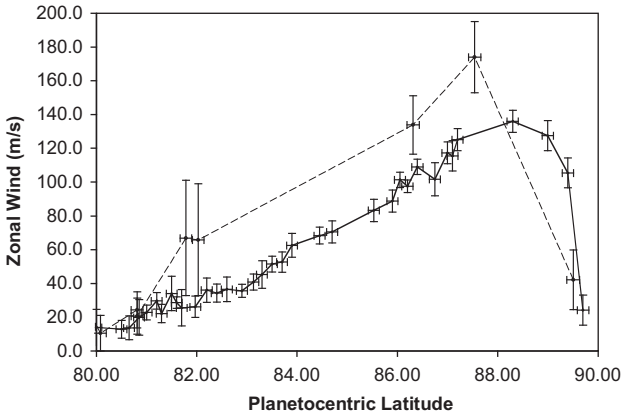

Fig. 8. Latitudinal profiles of the north and south polar zonal winds. Zonal winds measured from 5.1 μm images show similar cyclonic structures at both the northern (solid curve) and southern (dashed curve) poles. South polar wind data from Dyudina et al. (2009).

(Fletcher et al., 2008). Progressing equatorward, these winds die down to minima <15 m/s at 80.5°N and 80.1°S for the northern and southern cyclones, respectively.

3. Constraints on cloud altitudes

To provide constraints on the depths of the clouds observed in silhouette against the 5.1 μm internal glow of Saturn, we have examined the spectral behavior of candidate cloud morphologies

Table 3
Comparison of north vs. south polar cyclones.

Characteristic	North cyclone	South cyclone
Latitude (pc) of maximum measured wind (°)	88.3	87.5
Maximum wind (m/s)	136.0±6.5	174.0±21.1
Central eye wind (m/s)	24.3±8.9	42.2±17.7
Central eye latitude	89.7	89.5
Latitude (pc) of minimum measured wind (°)	80.5	80.1
Minimum windspeed	12.9±1.0	10.5±4.4
Eye Latitudinal shear (cm/s/km)	−25.8±5.9	−6.4±1.3
Mean latitudinal shear 82–87° (cm/s/km)	1.8±0.2	1.9±0.7

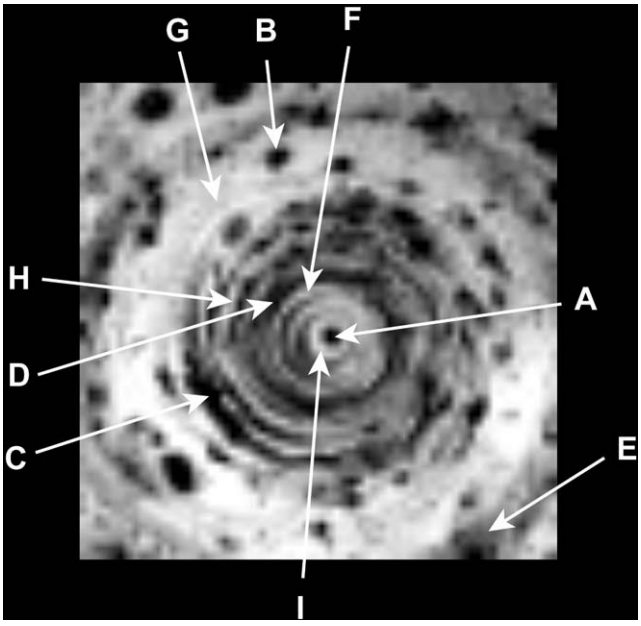

Fig. 9. North polar feature identification. Depicted are the nine 5-μm-dark clouds and 5-μm-bright clearings modeled with the NEMESIS radiative transfer code.

with the NEMESIS radiative transfer and retrieval code (Irwin et al., 2008). In particular, we examined two types of cloud morphologies. First, we examined a two-cloud model, wherein two physically thin but potentially optically thick clouds were placed at two different levels in the atmosphere. In the upper troposphere, a putative ammonia (NH_3) cloud was placed at 1.4-bar, the condensation level of ammonia pertaining to the solar mixing ratio of N/H (Atreya et al., 1999). Below this cloud, we placed a second, compact, putative ammonium hydrosulfide (NH_4SH) cloud for which the precise pressure level was determined by the spectral analysis, as were as well the 5 μm opacities of both clouds. A wavelength-independent extinction coefficient was adopted for both clouds.

In the second cloud morphology examined in our study, we assumed a single physically and optically thick cloud for which the cloudbase and 5 μm opacity are determined by the observations. In this model, the cloud was assumed to extend from its cloudbase upward to the 75-mbar level, with a uniform vertical distribution of opacity with pressure (i.e., equivalent to a particle-to-gas scale-height ratio of unity).

We analyzed nine specific spectra consisting of five 5-μm-dark cloudy and four 5-μm-bright less opaque regions denoted in Fig. 9. Fig. 10 shows representative results for three cloudy regions, depicting the best-model fits and the variation of χ^2 for each of the two morphologies. As a function of deep-cloud pressure, the fitting parameter, χ^2, diminishes greatly for deep clouds below the 2- and 3-bar level for the two-cloud and single-cloud model, respectively. Best-fit results for all nine regions are shown in Table 4. For both morphologies, and for all regions analyzed, each of our analyses demands an optically thick cloud in the lower troposphere at and below the 2.1- and 3.9-bar pressure level for the two-cloud and single-cloud model, respectively. For the deep cloud, there are distinct dichotomies between cloudy and relatively clear regions, as noted in the bottom rows of Table 4 and shown graphically in Fig. 11. For both morphologies, the 5-μm opacity of cloudy regions is twice that of relatively clear regions. In the two-cloud model, the deep optically thick cloud is about 0.5 bar higher in altitude in 5-μm-dark regions than in less opaque 5-μm-bright regions. In contrast, for the single-cloud morphology, the base of the deep cloud is about 0.7 bar deeper in cloudy vs. relatively clear regions, i.e., at ~4.7 vs. ~4.0 bar in cloudy vs. relatively clear regions.

In the two-cloud model, similar 5-μm opacities are found for the upper cloud in both cloudy and relatively clear regions, i.e., ~0.57 and ~0.84 for the 5-μm-dark and bright regions, respectively. Thus, the two-cloud morphology suggests that a relatively uniform cloud layer covers the north polar region, whose opacity is a factor of 4–8 less than the underlying deep cloud. While we modeled this relatively optically thin cloud as occurring at the 1.4-bar ammonia condensation level, our analysis does not constrain the altitude. Thus, this nearly uniform cloud layer could be almost anywhere above the 1.4-bar level. As the sun rises over this region in 2009, the altitude, visual opacity, and other characteristics of the upper-level cloud layer should be discernable in both VIMS spectral imagery and Imaging Sub-System (ISS) images multi-filter images.

In summary, our spectral analysis of two distinct cloud morphologies indicates that 5-μm optically thick clouds are located relatively deep in the atmosphere, at or below the 2.1-bar level, at depths below the ammonia condensation level. Thus, these deep clouds are not comprised of ammonia, but rather likely either ammonia hydrosulfide and/or water, the next two condensibles predicted for the deep atmosphere of Saturn (Weidenschilling and Lewis, 1973; Atreya et al., 1999).

4. Dynamical implications and conclusion

The north polar cyclone together with its southern counterpart (Dyudina et al., 2008) are the first two polar cyclonic features discovered in the giant atmospheres of the outer solar system. Cyclones exist at both poles of Venus (e.g., Suomi and Limaye, 1978; Limaye, 2007; Limaye et al., 2009), and polar vortices have been observed on Mars and Earth as well. The high-latitude jets on Neptune, which peak at a latitude of ~70°, could perhaps be viewed as circumpolar vortices, although they are much larger in latitudinal extent than the polar vortex identified here. Thus, large cyclonic features appear to be not an uncommon dynamical mode of polar dynamics in planets with significant atmospheres.

To investigate the two-dimensional dynamical stability of the north polar region, we examined the two-dimensional stability criterion which compares the second meridional derivative of zonal velocity, u_{yy}, with the meridional derivative of the Coriolis force (df/dy, or β). For more accurate analysis of differentials over small distances and with non-insignificant error bars, we smoothed the zonal velocity curve of Fig. 3 using spline fits and the hexagonal zonal winds shown in Fig. 5. Fig. 12 shows the resulting smoothed zonal-wind profile for the north polar region, while Fig. 13 shows the resulting latitudinal profile of u_{yy} compared to β. Over much of the region, u_{yy} exceeds β by more than an order of magnitude, consistent with earlier inferences from Voyager observations (Godfrey, 1988; Allison et al., 1990).

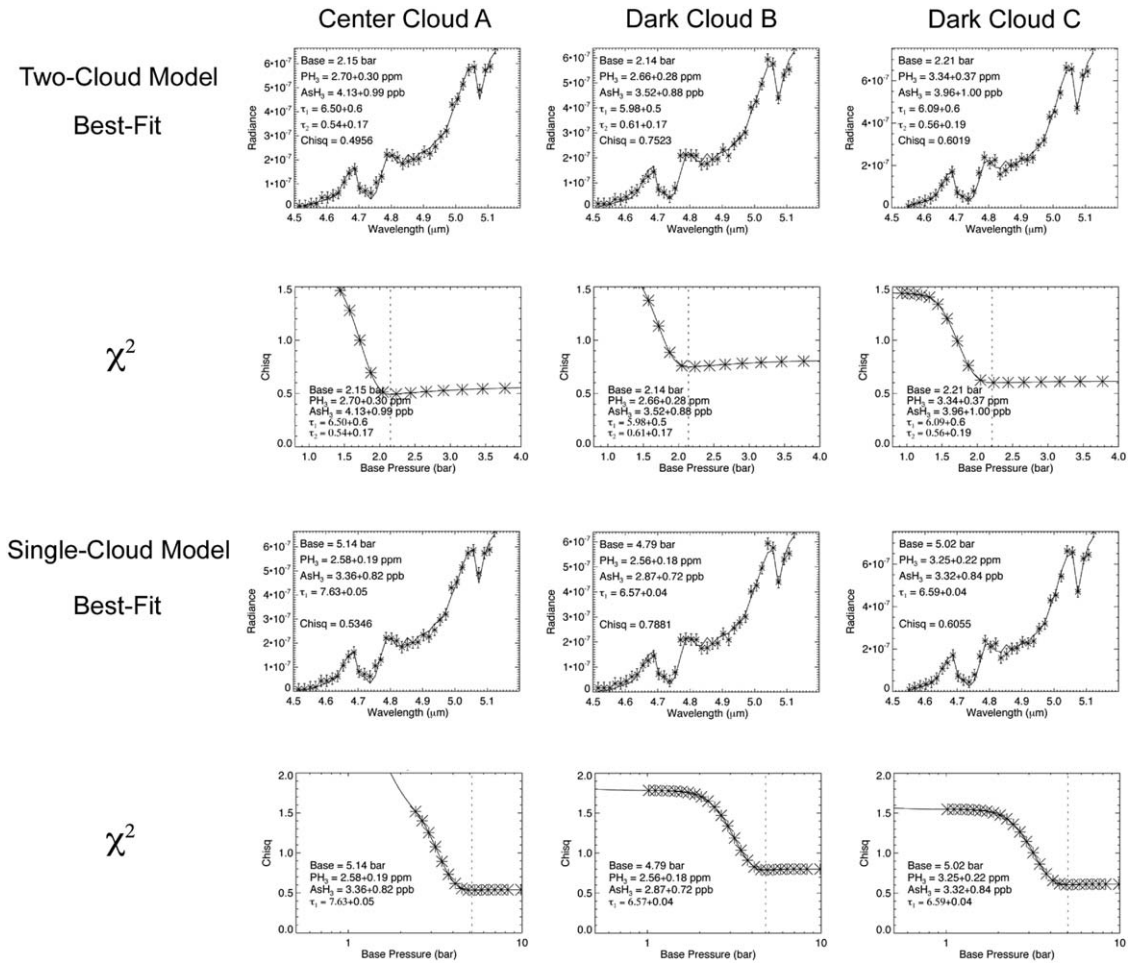

Fig. 10. Best fit models and χ^2 vs. deep cloudbase pressure. Results for three clouds noted in Fig. 9 are shown for both two-cloud and single-cloud models.

Table 4
North polar clouds characteristics from 5-μm modeling.

Feature ID	Cloud/clearing	Two-cloud model results				Single-cloud model results		
		Lower cloud		Upper cloud		Extended cloud		
		Pressure (bar)	5.1 μm opacity	5.1-μm opacity	Best-fit χ^2	Cloud base (bar)	5.1 μm opacity	Best-fit χ^2
A	Center Cloud	2.15	6.50±0.6	0.54±0.17	0.497	5.14	7.63±0.06	0.535
B	Cloud	2.14	5.98±0.5	0.61±0.17	0.752	4.79	6.57±0.04	0.788
C	Cloud	2.21	6.09±0.6	0.56±0.19	0.602	5.02	6.59±0.04	0.607
D	Cloud	2.3	5.02±0.5	0.55±0.23	0.763	4.27	4.85±0.03	0.781
E	Cloud	2.14	5.98±0.5	0.61±0.17	0.752	4.42	4.30±0.03	0.862
F	Clearing	2.68	2.58±0.7	0.88±0.37	1.177	3.93	3.18±0.03	1.18
G	Clearing	2.63	2.43±0.7	0.82±0.36	1.126	3.9	3.00±0.02	1.13
H	Clearing	2.63	2.56±0.7	0.88±0.37	1.032	3.9	3.17±0.02	1.036
I	Clearing	2.78	2.68±0.7	0.79±0.35	1.171	4.09	3.25±0.03	1.17
Mean								
Overall		2.41±0.27	4.42±1.81	0.69±0.15		4.38±0.49	4.73±1.78	
Cloud		2.19±0.07	5.91±0.54	0.57±0.03		4.73±0.38	5.99±1.37	
Clearing		2.68±0.07	2.56±0.10	0.84±0.04		3.96±0.09	3.15±0.11	

These inferences indicate that the hexagon and cyclone are not shallow dynamical features that can be characterized by the two-dimensional dynamical theory. Instead, the vertical dimension must be taken into account when assessing physical phenomena responsible for these features.

The discrete, localized nature of clouds observed throughout the north polar region indicates that if clouds are physically thick – as indicated by the high-altitude-probing sunlit glimpses of these clouds shown in Fig. 6 – then there is little vertical shear in the zonal winds on 1000 km scales. A significant shear could rapidly elongate the clouds, destroying their compact, nearly circular, appearance. Thus, our single-cloud model suggests that winds are nearly constant with altitude in the 1–3-bar region at and near the north pole on 1000 km scales. We note, however, that

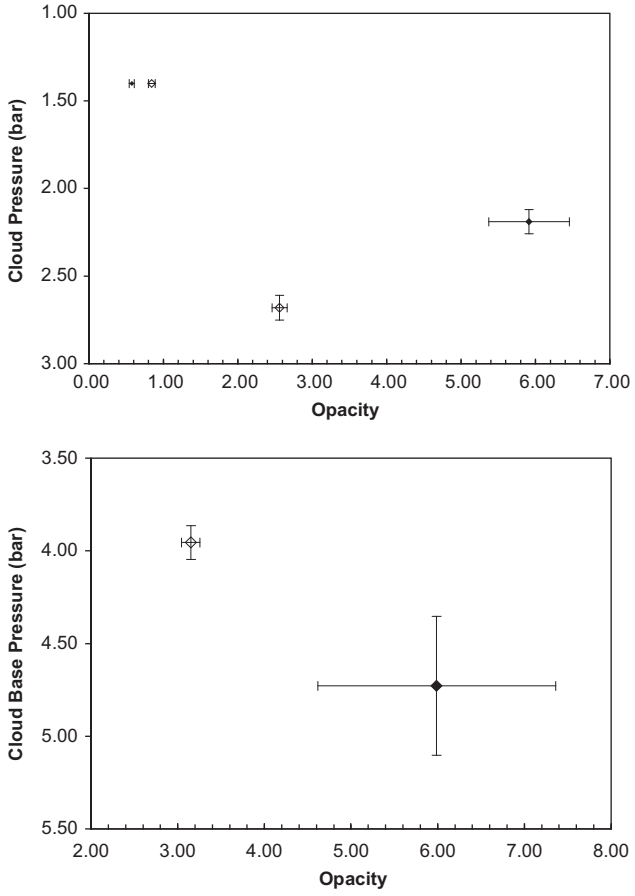

Fig. 11. Summaries of two-cloud (upper panel) and single-cloud (lower panel) models. Mean cloudbase pressure and opacity for cloudy (solid diamonds) and relatively clear (open diamonds) regions. Error bars show standard deviation of opacity and pressure among the five cloudy and four relatively clear regions analyzed.

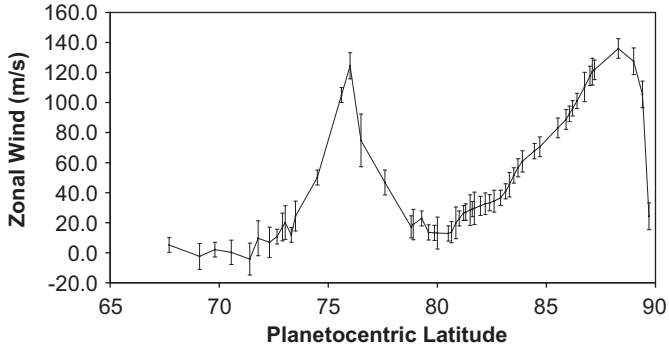

Fig. 12. Smoothed zonal-wind profile, used to derive u_{yy} shown in Fig. 13.

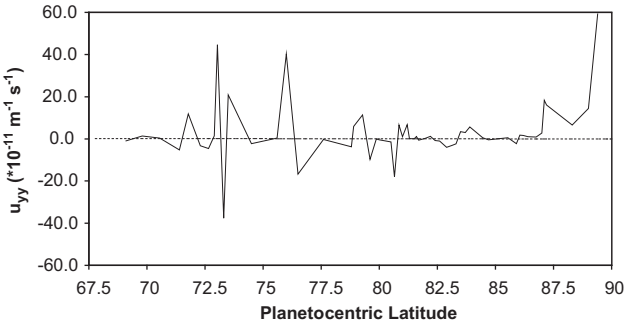

Fig. 13. Latitudinal profile of u_{yy} (solid) compared to the profile for β (dashed). $\beta < 0.2 \times 10^{-11}\,\mathrm{m^{-1}\,s^{-1}}$ throughout; thus, for 2-dimensional circulation/dynamics, the upper half of the figure represents an unstable dynamical region.

vortices are nonlinear coherent structures, and their nonlinearity could potentially help them survive as vertically extended structures even in the presence of moderate vertical shear; future modeling work will be needed to quantify this possibility. Further evidence of a vertically coherent wind structure comes from the Cassini/CIRS analysis of winds in the region derived from the thermal wind equation. Our direct measurement of a high-speed zonal jet maximum near 88°N with large zonal shears to its north and south at the ~2-bar level is consistent with the Cassini/CIRS predictions at higher altitudes – roughly, 1.5 bar above our measurement level – of a high-speed jet at 88°N and large latitudinal wind shears (Fletcher et al., 2008). Thus, the CIRS and VIMS results indicate a consistent cyclonic morphology with maximum winds near 88°N over a wide range of altitudes, from approximately the upper reaches of the CIRS measurements near 0.1 bar down to the several bar level of the VIMS measurements.

The circular cloud features themselves may be anticyclonic vortices, which can be generated by a variety of processes including baroclinic or barotropic instability, roll-up of small-scale turbulence, and convective events (Vasavada and Showman, 2005). Powerful moist-convective storms, presumably driven by buoyancy associated with latent heat release near the ~20-bar water condensation level (Weidenschilling and Lewis, 1973), have been observed on Saturn (e.g., Porco et al., 2005; Del Genio et al., 2007; Baines et al., 2009) and provide another possible generation mechanism for vortices. On Earth, moist convection transports a large fraction of the tropospheric heat flux in the tropics, yet such storms likewise cover only a small fractional area of the region. Given Saturn's even smaller heat flux (~5 W m^{-2} as compared to the mean absorbed energy flux of ~300 W m^{-2} in Earth's tropics), such active moist-convective storms should cover an even smaller fractional area on Saturn than on Earth. Adopting the mixing-length arguments from Lunine and Hunten (1987) with Saturn parameters suggests that the fractional area covered by active moist-convective updrafts should be ~10^{-5}–10^{-6}. Anvils, which may form when updraft air spreads laterally at the neutrally buoyant level near the tropopause, will cause the fractional area of the storm *clouds* to exceed that of the active *updrafts* that feed them. Nevertheless, we expect active storm clouds (i.e., those fed by active updrafts) to cover a fractional horizontal area of $\gamma \sim 10^{-2}$ or less. Since the small spots seen in VIMS images cover a substantial fraction of the total area in those latitude bands, moist convection can only account for most of these spots if the anvil clouds generated by moist convection have extended lifetimes of at least γ^{-1} or ~100 times longer than the active storm lifetimes, which requires lifetimes exceeding an Earth year for a typical active storm lifetime of a few days. In fact, coherent vortices have been observed to result from active storms on Saturn (Porco et al., 2005). However, most active storms on Jupiter and Saturn do not generate long-lived vortices but rather generate anvil clouds that are sheared apart by the ambient winds on timescales of days. Together, the above arguments suggest that it is unlikely that moist-convection events are the predominant formation mechanism for the small spots seen in VIMS images. Nevertheless, even if only a small fraction of the observed circular cloud features in the north polar region results from moist convection, it would suggest the possibility of a major role for such convection in delivering energy to the polar cyclone and its environs. New observations

expected from the high-resolution ISS camera system onboard Cassini should reveal much about the true nature of these features as the sun rises over the north polar region in 2009.

The north polar hexagon has now been observed repeatedly for 27.6 years, corresponding to nearly a Saturnian year (29.4 years). Voyager observations in November 1980 and August 1981 (Godfrey, 1988), ground-based observations in June, 1989 (Sánchez-Lavega et al., 1993), and repeated Cassini/VIMS and Cassini/CIRS observations since October, 2006 (Baines et al., 2007; Fletcher et al., 2008), have all shown the presence of the hexagonal feature. Both the long-term nature of the hexagon and its presence deep in the atmosphere at altitudes below the 2-bar level indicate that this feature is not a consequence of solar insolation effects but rather is associated with the global, non-seasonal circulation of Saturn.

The formation mechanism for the hexagon remains unclear. Allison et al. (1990) suggested that a planetary (i.e., westward-propagating Rossby) wave mechanism is responsible, wherein perturbations to the zonal flow induced by a large dark spot observed 3° south of the hexagon (Godfrey, 1988) serves to cause wavenumber 6 Rossby wave oscillations in the flow which appear as the straight-legged sides and curved corners of the high-latitude hexagon. This large (6000 km wide) dark spot was observed repeatedly over the years by Voyager in 1980/1981 (Godfrey, 1988), ground-based imagery in 1990/1991 (Sánchez-Lavega et al., 1993), and 1992–1995 (Sánchez-Lavega et al., 1997). However, this feature does not appear in the high-resolution images presented here, nor in the Cassini/CIRS observations of March 2007 (Fletcher et al., 2008), nor in any VIMS imagery of the north pole obtained during the mission beginning in October 2006 (Baines et al., 2007 and Figs. 1,2). The apparent longevity of the hexagon in absence of the dark spot, thus, raises the possibility that the dark spot was a by-product of hexagon formation (or perhaps even an unrelated feature altogether) rather than a cause of the hexagon.

Alternatively, it is possible that the hexagon results from an instability of the flow at the hexagon latitude. Laboratory experiments motivated by Saturn's hexagon (Aguiar et al., 2009), and numerical studies of terrestrial hurricanes (Schubert et al., 1999; Kossin and Schubert, 2001) show success in producing polygons from a barotropic instability. Such an instability is a horizontal shear instability that would convert kinetic energy of a pre-existing fast jet (as exists at the hexagon latitude) into eddy kinetic energy associated with the hexagon wave. Alternatively, it may be possible for the hexagon to result from a baroclinic instability if latitudinal temperature gradients exist at the hexagon latitude. Such instabilities, which would convert potential energy into kinetic energy, could help to pump the fast hexagon jet in addition to creating the hexagon wave. (An analogous mechanism was proposed for Saturn's Ribbon wave by Godfrey and Moore, 1986.) Numerical simulations of baroclinic instabilities on gas giants show that such instabilities can indeed pump zonal jets (Lian and Showman, 2008; Williams, 2003) and in some cases lead to wave structures on those jets that could appear polygonal if viewed from over the pole (Williams, 2003). Note that both types of instabilities can also produce coherent vortices and thus could provide the explanation for the adjacent dark spot seen in Voyager, ground-based, and early Cassini imagery.

Acknowledgments

We thank Cassini/VIMS team members John Ivens, Frank Leader, Dyer Lytle, Dan Moynihan, Virginia Pasek, Alan Stevenson, and Bob Watson for much help in the sequence generation, instrument calibration, and data reduction of the maps and spectra used in this paper. We would like to thank Anthony Del Genio and an anonymous referee for their valuable comments. Much of the work described in this paper was carried out in part at the Jet Propulsion Laboratory, Pasadena, California, under contract with the National Aeronautics and Space Administration. LNF was supported by an appointment to the NASA Postdoctoral Program at the Jet Propulsion Laboratory, administered by Oak Ridge Associated Universities through a contract with NASA. We thank Patrick Irwin and colleagues for the use of the Oxford-based radiative transfer and retrieval code.

References

Aguiar, A.C.B., Read, P.L., Salter, T., Wordsworth, R.D., Yamazaki, Y.H., 2009. A laboratory model of Saturn's north polar hexagon. Icarus, submitted.

Allison, M., Godfrey, D.A., Beebe, R.F., 1990. A wave dynamical interpretation of Saturn's polar hexagon. Science 247, 1061–1063.

Atreya, S.K., Wong, M.H., Owen, T.C., Mahaffy, P.R., Niemann, H.B., de Pater, I., Drossart, P., Encrenaz, T., 1999. A comparison of the atmospheres of Jupiter and Saturn: Deep atmospheric composition, cloud structure, vertical mixing, and origin. Planet. Space Sci. 47, 1243–1262.

Baines, K.H., Momary, T.W., Temma, T., Buratti, B.J., Roos-Serote, M., Showman, A., Brown, R.H., Clark, R.N., Nicholson, P.D., Atreya, S.K., Graham, J., Marquez, E., 2007. The structure of Saturn's poles determined by Cassini/VIMS: Constraints on winds and horizontal and vertical cloud distributions. Bull. Amer. Astr. Soc. 38, 423.

Baines, K.H., Delitsky, M.L., Momary, T.W., Brown, R.H., Buratti, B.J., Clark, R.N., Nicholson, P.D., 2009. Storm clouds on Saturn: Lightning-induced chemistry and associated materials consistent with Cassini/VIMS spectra. Planet. Space Sci, this issue, doi:10.1016/j.pss.2009.06.025.

Barnes, J.W., Brown, R.H., Soderblom, L., Buratti, B.J., Sotin, C., Rodriguez, S., Le Mouelic, S., Baines, K.H., Clark, R., Nicholson, P., 2007. Global-scale surface spectral variations on Titan seen from Cassini/VIMS. Icarus 186, 242–258.

Bevington, P.R., 1969. Data Reduction and Error Analysis for the Physical Sciences. McGraw Hill, New York, pp. 104–105.

Brown, R.H., 21 Colleagues, 2004. The Cassini visual and infrared mapping spectrometer investigation. Space Sci. Rev. 115 (1–4), 111–168.

Choi, D.S., Showman, A.P., Brown, R.H., 2009. Cloud features and zonal wind measurements of Saturn's atmosphere as observed by Cassini/VIMS. J. Geophys. Res., doi:10.1029/2008JE003254.

Del Genio, A.D., Coauthors, 2007. Saturn eddy momentum fluxes and convection: first estimates from Cassini images. Icarus 189, 479–492, doi:10.1016/j.icarus.2007.02.013.

Desch, M.D., Kaiser, M.L., 1981. Voyager measurements of the rotation period of Saturn's magnetic field. Geophys. Res. Lett. 8, 253–256.

Dyudina, U.A., Ingersoll, A.P., Ewald, S., Vasavada, A., West, R.A., Del Genio, A., Barbara, J., Porco, C.C., Achterberg, R., Flasar, F., Simon-Miller, A., Fletcher, L.N., 2008. Dynamics of Saturn's south polar vortex. Science 319, 1801.

Dyudina, U.A., Ingersoll, A.P., Ewald, S.P., Vasavada, A.R., West, R.A., Baines, K.H., Momary, T.W., Del Genio, A.D., Barbara, J.M., Porco, C.C., Achterberg, R.K., Flasar, F.M., Simon-Miller, A.A., Fletcher, L.N., 2009. Saturn's south polar vortex compared to other large vortices in the solar system. Icarus 202, 240–248.

Fletcher, L.N., Irwin, P.G.J., Orton, G.S., Tenby, N.A., Achterberg, R.K., Bjoraker, G.L., Read, P.L., Simon-Miller, A.A., Howett, C., de Kok, R., Bolwes, N., Calcutt, S.B., Hesman, B., Flasar, F.M., 2008. Temperature and composition of Saturn's polar hot spots and hexagon. Science 319, 70–82.

Gaddis, L., et al., 1997. An overview of the Integrated Software for Imaging Spectrometers (ISIS), Lunar and Planetary Institute Conference Abstracts, 28, 387.

Godfrey, D.A., 1988. A hexagonal feature around Saturn's north pole. Icarus 76, 335–356.

Godfrey, D.A., Moore, V., 1986. The Saturnian ribbon feature—a baroclinically unstable model. Icarus 68, 313–343.

Irwin, P.G.J., Teanby, N.A., de Kok, R., Fletcher, L.N., Howett, C.J.A., Tsang, C.C.C., Wilson, C.F., Calcutt, S.B., Nixon, C.A., Parrish, P.D., 2008. The NEMESIS planetary atmosphere radiative transfer and retrieval tool. J. Quant. Spectrosc. Radiative Transfer 109, 1136–1150.

Kossin, J.P., Schubert, W.H., 2001. Mesovortices, polygonal flow patterns, and rapid pressure falls in hurricane-like vortices. J. Atmos. Sci. 58, 2196–2209.

Lian, Y., Showman, A.P., 2008. Deep jets on gas-giant planets. Icarus 194, 597–615, doi:10.1016/j.icarus.2007.10.014.

Limaye, S.S., 2007. Venus atmospheric circulation: known and unknown. J. Geophys. Res. 112, E04S09, doi:10.1029/2006JE002814.

Limaye, S.S., Kossin, J.P., Rozoff, C., Piccioni, G., Titov, D.V., Markiewicz, W.J., 2009. Vortex circulation on Venus: Dynamical similarities with terrestrial hurricanes. Geophys. Res. Lett. 36, L04204, doi:10.1029/2008GL036093.

Lunine, J.I., Hunten, D.M., 1987. Moist convection and the abundance of water in the troposphere of Jupiter. Icarus 69, 566–570.

Porco, C.C., 31 Colleagues, 2005. Cassini imaging science: initial results on Saturn's atmosphere. Science 307, 1243–1247.

Read, P.L., Conrath, B.J., Fletcher, L.N., Gierasch, P.J., Simon-Miller, A.A., Zuchowski, L.C., 2009. Mapping potential vorticity dynamics on Saturn: zonal mean

circulation from Cassini and Voyager data. Plane. Space Sci., this issue, doi:10.1016/j.pss.2009.03.004.
Sánchez-Lavega, A., Lecacheux, J., Colas, F., Lacques, P., 1993. Ground-based observations of Saturn's North Polar spot and hexagon. Science 260, 329–332.
Sánchez-Lavega, A., Rojas, J.F., Acarreta, J.F., Lecacheux, J., Colas, F., Sada, P.V., 1997. New observations and studies of Saturn's long-lived North Polar spot. Icarus 128, 322–334.
Schubert, W.H., Montgomery, M.T., Taft, R.K., Guinn, T.A., Fulton, S.R., Kossin, J.P., Edwards, J.P., 1999. Polygonal eyewalls, asymmetric eye contraction, and potential vorticity mixing in hurricanes. J. Atmos. Sci. 56, 1197–1223.
Suomi, V.E., Limaye, S.S., 1978. Venus: further evidence of vortex circulation. Science 201, 1009–1011.
Vasavada, A.R., Showman, A.P., 2005. Jovian atmospheric dynamics: an update after Galileo and Cassini. Rep. Prog. Phys. 68, 1935–1996.
Weidenschilling, S.J., Lewis, J.S., 1973. Atmospheric and cloud structures of the Jovian planets. Icarus 20, 465–476.
Williams, G.P., 2003. Jovian dynamics, part III: multiple, migrating, and equatorial jets. J. Atmos. Sci. 60, 1270–1296.